Assessing the Ducting Phenomenon and its Potential Impact on GNSS Radio Occultation Refractivity Retrievals over the Northeast Pacific Ocean using Radiosondes and Global Reanalysis

Thomas E. Winning Jr. [1], Feiqin Xie[1] and Kevin J. Nelson[1,a]

[1] Texas A&M University – Corpus Christi, Corpus Christi, 78412, USA

[a] now at: Jet Propulsion Laboratory, California Institute of Technology, Pasadena, 91109, USA

Correspondence to: Thomas E. Winning Jr. (twinning@islander.tamucc.edu)

Abstract. In this study, high-resolution radiosondes from the MAGIC field campaign and ERA5 global reanalysis data are used to assess the elevated ducting layer characteristics along the transect over the northeastern Pacific Ocean from Los Angeles, California to Honolulu, Hawaii. The planetary boundary layer height (PBLH) increases as the strength of the refractivity gradient decreases westward along the transect. The thickness of the prevailing ducting layer remains remarkably consistent (~110 m) in the radiosonde data. On the other hand, the ERA5 generally resolves the ducting features well but underestimates the ducting height and strength especially over the trade cumulus region near Hawaii. A simple two-step end-to-end simulation is used to evaluate the impact of the elevated ducting layer on RO refractivity retrievals. A systematic negative refractivity bias (*N*-bias) below the ducting layer is observed throughout the transect, peaking (−5.42%) approximately 80 meters below the PBL height, and gradually decreasing towards the surface (−0.5%). The *N*-bias shows strong positive correlation with the ducting strength. The ERA5 data underestimate the *N*-bias with the magnitude of the underestimation increasing westward along the transect.

1   Introduction

The troposphere, where most weather occurs, consists of two main layers: the planetary boundary layer (PBL) and the free atmosphere (FA) (Garratt, 1994). The PBL characteristics change frequently on both spatial and temporal scales and the PBL height (PBLH) can impact the exchange of heat, momentum, and particulate matter with the FA, making it a critical factor in global energy balances and water cycling (Stull 1988; Ramanathan et al. 1989; Klein and Hartmann 1993). Regular PBL observations are mainly limited to in situ measurements from surface stations and radiosondes. However, spatially and temporally dense in situ PBL observations are only available from field campaigns such as the Boundary Layer Experiment 1996 (BLX96, Stull et al. 1997), the Variability of the American Monsoon Systems (VAMOS) Ocean-Cloud-Atmosphere-Land Study Regional Experiment (VOCALS-REx, Wood et al. 2011), and the Marine Atmospheric Radiation Measurement (ARM) Global Energy and Water Experiment (GEWEX) Cloud System Studies (GCSS) Pacific Cross Section Intercomparison (GPCI) Investigation of Clouds (MAGIC, Zhou et al. 2015). Satellite observations of the PBL are also limited due to signal attenuation of the conventional infrared sounder in the lower troposphere and the low vertical resolution of microwave sounding instruments. Additionally, while the depth of the PBLH can vary from a couple hundred meters to a few kilometers (von Engeln and Teixeira 2013; Ao et al. 2012), the transition layer from the PBL to the FA is typically on the order of tens to hundreds of meters thick (Maddy and Barnet 2008), rendering ineffective PBL sensing from the low vertical resolution passive infrared and microwave sounders.

On the other hand, Global Navigation Satellite System (GNSS) radio occultation (RO) provides global atmospheric soundings with a vertical resolution of approximately 100 m in the lower troposphere under all weather conditions (Gorbunov et al., 2004; Kursinski et al., 2000, 1997). One of the major GNSS RO missions is the Formosat-3/Constellation Observing System for Meteorology, Ionosphere, and Climate (COSMIC), later referred to as COSMIC-1 (Anthes et al. 2008), and its follow-on mission COSMIC-2 (Schreiner et al. 2020). Numerous studies have documented the high value of GNSS RO for profiling the PBL and determining the PBLH (Nelson et al. 2021; Winning et al. 2017; Ho et al. 2015; Ao et al. 2012; ; Guo et al. 2011; Basha and Ratnam 2009; Ao et al. 2008; Xie et al. 2008).

The advancement of the GNSS RO technique with open-loop tracking (Sokolovskiy et al., 2006; Beyerle et al., 2003; Ao et al., 2003) along with the implementation of the radio-holographic retrieval algorithm (Jensen et al., 2004; Jensen et al., 2003; Gorbunov, 2002) have led to much improved PBL sounding quality. However, probing the marine PBL remains challenging as systematic negative biases are frequently seen in RO refractivity retrievals (Feng et al. 2020; Xie et al. 2010). One major cause of the refractivity bias (hereafter N-bias) is the RO retrieval error due to elevated atmospheric ducting often seen near the PBLH (Ao et al., 2007; Xie et al., 2006; Ao et al. 2003; Sokolovskiy 2003). This elevated ducting prevails over the subtropical eastern oceans (Feng et al., 2020; Lopez, 2009; von Englen et al., 2003), and the horizontal extent of ducting in these regions can be on the order of thousands of kilometers (Winning et al. 2017; Xie et al. 2010). In the presence of ducting, the vertical refractivity gradient exceeds the critical refraction threshold for L-band frequencies (i.e., $dN/dz \leq -157$ N-units km^{-1}). The steep negative refractivity gradient is often observed in the vicinity of the PBLH, which is typically caused by an atmospheric temperature inversion, a sharp decrease in moisture, or a combination of both. When ducting is present, the Abel inversion (e.g., Fjeldbo et al., 1971) in the standard retrieval process encounters a non-unique inversion problem due to a singularity in the bending angle, resulting in large, systematic underestimation of refractivity (N) below the ducting layer (Xie et al. 2006; Ao et al., 2003; Sokolovskiy, 2003). The large uncertainty in RO refractivity coupled with the singularity in bending angle hinders assimilation of RO observations into numerical weather models, resulting in discarding of a significant percentage of RO measurements inside the PBL (Healy, 2001).

To comprehensively assess the potential impact of ducting on GNSS RO retrievals, we begin by constructing a detailed ground truth of PBL ducting statistics. This is derived from an extensive set of high-resolution radiosonde data over the northeastern Pacific Ocean, a region known for prevailing ducting conditions. Subsequently, we conduct a simulation study using the radiosonde data to evaluate the N-biases caused by varying ducting characteristics. Section 2 provides details of the two data sets used for this study: high-resolution radiosondes over the northeastern Pacific Ocean and the colocated ECMWF Reanalysis version 5 (ERA5, Hersbach et al. 2020) profiles. Additionally, we discuss the co-location criteria and the detection method for ducting layer and the corresponding PBLH. Section 3 presents the ducting statistics for key variables, such as ducting height, PBLH, minimum refractivity gradient, and sharpness parameter. The

91 characteristics of ducting including the thickness and strength along the cross-section are also

92 shown. Furthermore, we evaluate the ducting-induced N-bias in GNSS RO refractivity retrievals

93 by carrying out a two-step end-to-end simulation. Section 4 summarizes the findings and

94 discusses the direction of future research.

95 **2   Data and methods**

96 **2.1 MAGIC radiosonde and colocated ERA5 data**

97 A collection of high-resolution radiosondes from the Marine Atmospheric Radiation

98 Measurement (ARM) GCSS Pacific Cross Section Intercomparison (GPCI) Investigation of

99 Clouds (MAGIC) are utilized as the primary data set in this analysis (Lewis 2016; Zhou et al.

100 2015). The MAGIC field campaign took place from 26 September 2012 to 2 October 2013 as

101 part of the U.S Department of Energy ARM Program Mobile Facility 2 (AMF2) aboard the

102 Horizon Lines container ship, *Spirit*, which completed 20 round trip passes between Los

103 Angeles, California and Honolulu, Hawaii during the yearlong data collection period (Painemal

104 et al., 2015; Zhou, 2015). During each transit, radiosondes were launched at 6-hour intervals

105 from the beginning of the program through the end of June 2013; the observation frequency

106 increased to every 3 hours from July 2013 through the end of the campaign (Zhou et al., 2015).

107 A total of 583 MAGIC radiosonde profiles were collected during the field campaign (Zhou et al.,

108 2015), all with a vertical sampling frequency of 0.5 Hz (2 seconds), which provides an average

109 vertical resolution of ~8 m below 3 km, but varies due to local vertical motion.

110 Use of this data set serves multiple benefits. First, the northeast Pacific transitions from a

111 shallow stratocumulus-topped PBL to a higher, trade-cumulus boundary layer regime along the

112 GPCI transect (Garratt, 1994). Second, the large number of observations over a 12-month time

113 frame provides high temporal (diurnal and seasonal) and spatial profiling of the PBL along the

114 GPCI transect seen in Fig.1. Finally, ducting is prevalent throughout the domain which creates a

115 natural cross-section of refractivity field in X (zonal) and Z (vertical) dimensions.
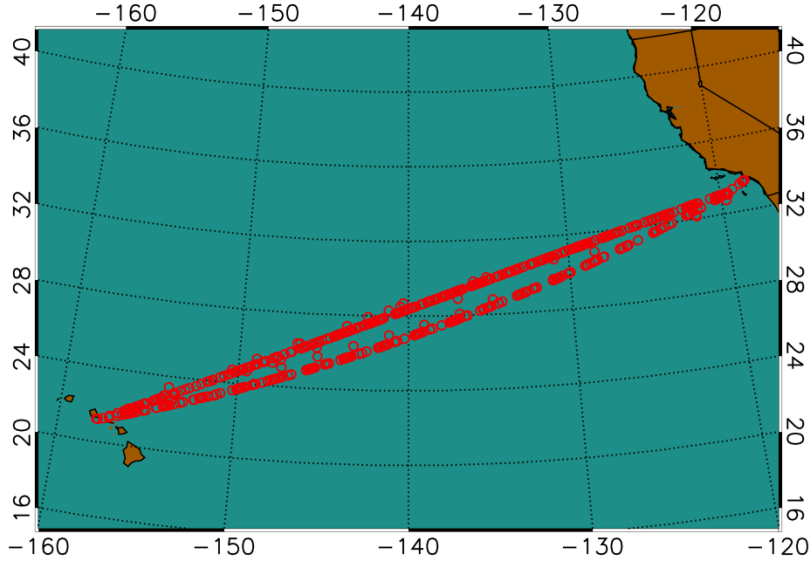
Figure 1: Location of radiosonde observations from the MAGIC field campaign October 2012–September 2013.

The radiosonde profiles are colocated with ERA5 model reanalysis profiles. The ERA5 reanalysis data have a horizontal grid resolution of 0.25˚x0.25˚, 1-hour temporal resolution, and 137 uneven vertical model levels from the surface to 0.01 hPa. The model level density decreases with height: on average, there are 19 model levels below 1 km (10 –100 m resolution), which reduces to 8 levels between 1 and 2 km (100 − 160 m resolution), and further reduces to 5 levels between 2 and 3 km (160-200 m resolution). Each MAGIC radiosonde profile was colocated with the nearest ERA5 grid point that is within 1.5 hours of the closest 3-hourly model reanalysis profile.

2.2 PBL height detection with the minimum gradient method

At GNSS L-band frequencies, the atmospheric refractivity (N in N-units) is derived from the refractive index n, where $N = (n - 1) \times 10^6$ and, in the neutral atmosphere (Kursinski et al., 1997), is a function of the atmospheric pressure (P in mb), temperature (T in K), and partial pressure of water vapor (P_w in mb) as seen in Eq. (1) from Smith and Weintraub (1953).

$$N = 77.6\frac{P}{T} + 3.73 \times 10^5 \frac{P_w}{T^2},$$
(1)

Over the subtropical eastern oceans, a sharp decrease in moisture is often associated with a strong temperature inversion marking a clear transition from the PBL to the FA. Both the distinct decrease in moisture and the temperature inversion lead to a sharp negative refractivity gradient which can be precisely detected from GNSS RO. Numerous studies have implemented the

137 simple gradient method to detect the PBLH, i.e., the height of the minimum refractivity gradient
138 (Ao et al., 2012; Seidal et al., 2010; Xie et al., 2006). To assess the robustness of PBLH
139 detection with gradient method, Ao et al. (2012) introduced the sharpness parameter ($\widetilde{N}^{'}$) to
140 measure the relative magnitude of the minimum gradient from surface to 5 km as follows:

141 $\widetilde{N}' \equiv -\frac{N'_{min}}{N'_{RMS}},$ (2)

142 Each refractivity gradient profile can then be filtered to identify the PBLH values with sharpness
143 parameter exceeding a specific threshold, thus increasing the robustness of PBLH detection. In
144 this study, the MAGIC radiosonde refractivity profiles were first interpolated to a uniform 10 m
145 vertical grid and then smoothed by a 100 m boxcar window to reduce the noise in the gradient
146 profile resulting from the high sampling rate. Moreover, the 100 m smoothed radiosonde will be
147 more consistent with the vertical resolution of GNSS RO measurements (e.g. Gorbunov et al.,
148 2004). Colocated ERA5 data were also vertically interpolated to the same 10 m grid but not
149 smoothed as these data do not contain the inherent noise as the radiosonde observations. In
150 addition, as the elevated ducting layer is the focus of this study, the lowest 0.3 km above mean-
151 sea-level of the *N*-profile near surface are excluded (e.g., Xie et al., 2012). Subsequently, the
152 height of the minimum refractivity gradient (within 0.3 km and 5 km) will be identified as the
153 PBLH.

154 **2.3 Ducting layers**

155 When the vertical refractivity gradient is less than the critical refraction ($\mathrm{d}N/\mathrm{d}z \approx -157.0$ *N*-units
156 km^{-1}), ducting occurs (Sokolovskiy, 2003). A ducting layer is identified as any interval of
157 continuous points with a vertical refractivity gradient equal to or less than -157 N-units km^{-1}.
158 Instances of multiple ducting layers occurring within a profile are present for both the MAGIC
159 (31.5%) and ERA5 (6.7%) data sets. In this study, we only recognize one dominant "ducting
160 layer" in each profile where the minimum vertical gradient is located. The ducting layer
161 thickness (Δh) is defined as the interval between the top and bottom of the ducting layer where
162 the refractivity gradients reach critical refraction. Similarly, the strength of each ducting layer
163 (ΔN) is defined as the refractivity difference between the bottom and top of the ducting layer.
164 The ducting layer height is in reference to the top of the ducting layer (Ao, 2007), which is
165 generally slightly above the PBLH.

166 Figure 2 shows vertical profiles of refractivity (N-units x 1/10, *N/10*), temperature (*T*), and

167 specific humidity (*q*) along with their respective vertical gradients (d*N*/dz, d*T*/dz and d*q*/dz) from

168 a representative MAGIC radiosonde (Fig. 2a,b) case located at (23.69˚N, −150.02˚E), and its

169 colocated ERA5 (Fig. 2c,d) profile at (23.75˚N, −150.00˚E). The PBLH of the radiosonde (2.10

170 km) is almost identical to the colocated ERA5 (2.14 km) and the "dominant" ducting layer near

171 the PBLH demonstrates similar thickness. However, a second, weaker ducting layer seen in the

172 radiosonde above the PBLH was not captured by the ERA5.
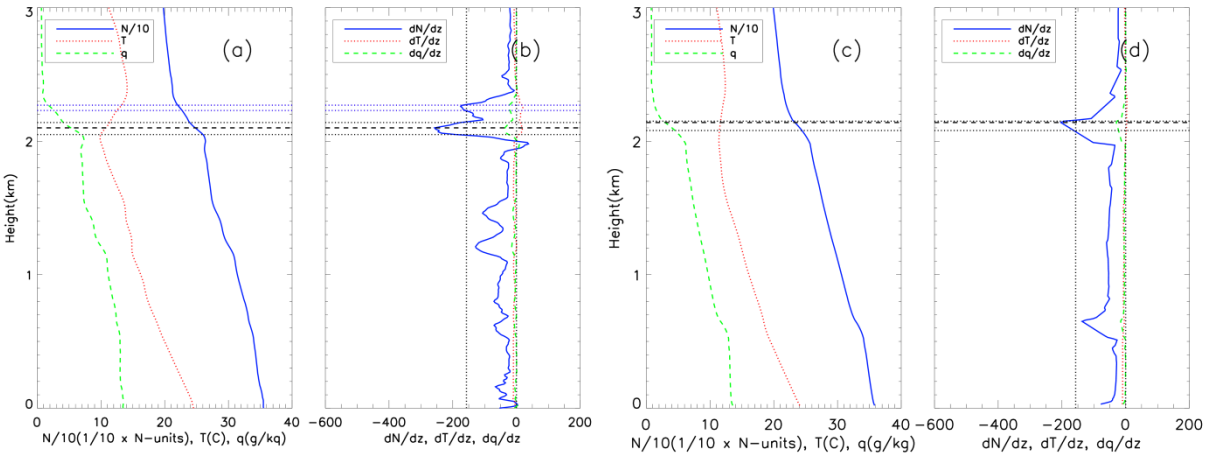
173

174 **Figure 2: Vertical profiles of refractivity (1/10 x N in *N*-units, *N/10*, solid blue), temperature (*T* in ˚C, dotted red) and**
175 **specific humidity (*q* in g kg^{-1}, dashed green) for (a) radiosonde at (23.69˚N, -150.02˚E) launched at 2012-10-02, 05:30**
176 **UTC, and (c) colocated ERA5 at (23.75˚N, -150.00˚E); and associated gradient profiles for radiosonde (b) and ERA5 (d).**
177 **The horizontal dashed line highlights the height of the minimum gradient, i.e., PBLH. The paired horizontal dotted lines**
178 **represent the bottom and top of the two ducting layers in the radiosonde profile (a and b) but only one in the ERA5**
179 **profile (c and d).**

180 **2.4 Evaluation of GNSS RO *N*-bias resulting from ducting**

181 In order to estimate the systematic negative *N*-bias in GNSS RO observations in the presence of

182 ducting, we use an end-to-end simulation on the radiosonde and ERA5 refractivity profiles. The

183 simulation consists of a two-step process adapted from Xie et al. (2006). The first step is to

184 simulate the 1-dimensional GNSS RO bending angle as a function of impact parameter (i.e., the

185 product of refractive index and the radius of the Earth's curvature) by forward Abel integration

186 of an input refractivity profile assuming a spherically symmetric atmosphere (Sokolovskiy, 2001;

187 Eshleman, 1973, Fjeldbo and Eshleman, 1968). The second step is to simulate the GNSS RO

188 refractivity retrieval by applying the Abel inversion on the simulated bending angle from step

189 one. In the absence of ducting, the impact parameter increases monotonically with height,

190 allowing a unique solution to the inverse Abel retrieval that is the same as the original

191 refractivity profile input. However, in the presence of an elevated ducting layer, the Abel

192 retrieval systematically underestimates the refractivity profile due to the non-unique Abel

193 inversion problem resulting from the singularity in bending angle across the ducting layer (Xie et

194 al., 2006; Sokolovskiy 2003). It should be noted that after the 100 m vertical smoothing on

195 radiosonde (no smoothing on ERA5) profiles as described in section 2.2, an additional 50 m

196 vertical smoothing has been applied to the simulated bending angle profiles of both radiosonde

197 and ERA5 data sets to alleviate the challenge of integration through the very sharp bending angle

198 resulting from ducting in the inverse Abel integration procedure (Feng et al., 2020).

199 Figure 3 shows the end-to-end simulation results for the same radiosonde (a–d) and the colocated

200 ERA5 (e–h) cases from Fig. 2. Figures 3a and 3e show refractivity profiles from the radiosonde

201 (N_{rds}) and the colocated ERA5 (N_{ERA5}) data as well as their corresponding Abel refractivity

202 retrievals (N_{Abel}). The PBLH is marked by a horizontal dotted line. The peak bending angle is

203 consistent with the sharp refractivity gradient. Figure 3b shows the fractional N-bias between the

204 simulated Abel retrieved RO refractivity profile and the observation, i.e., $((N_{Abel} - N_{Obs})/N_{Obs})$.

205 Considering the significant spatial and temporal variations of ducting height along the transect,

206 each N-bias profile is normalized to its PBLH for the purposes of comparison. For example, the

207 zero-adjusted height refers to the PBLH for each individual profile. The systematic negative N-

208 bias is clearly shown below the ducting layer marked by the PBLH in both cases, with the biases

209 decreasing at lower altitude, the largest magnitude bias (−5% for radiosonde; −2.5% for ERA5)

210 close to the ducting height and a minimum magnitude approaching zero near the surface.
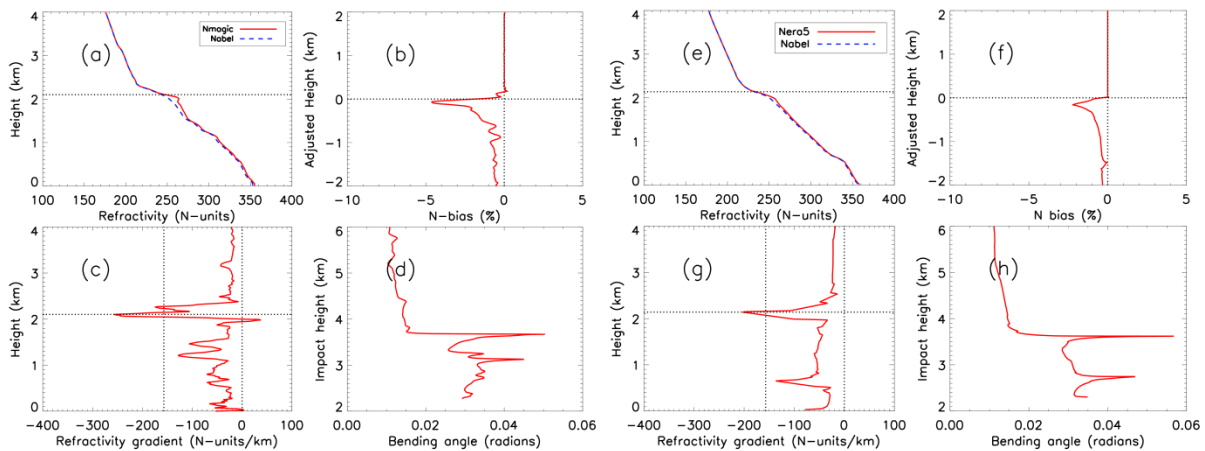
211

212 **Figure 3: End-to-end simulation data for MAGIC radiosonde launched at 0530 UTC on 20121002 showing: (a) N_{Obs} (solid**
213 **red) and N_{Abel} (blue dashed) from surface to 4 km; (b) PBLH adjusted N-bias $((N_{Abel} - N_{Obs})/N_{Obs})$; (c) refractivity gradient**
214 **and (d) bending angle vs. impact parameter. The same is shown in panels e-h for the colocated ERA5 profile.**

3   Analysis

Quality control for radiosonde (and colocated ERA5) profiles was based on five key criteria. First, a total of 19 radiosonde and 24 ERA5 profiles near the southern California coast were removed due to their positions east of $-120°$E or anomalously high PBL (PBLH > 3.0 km) with no distinct minimum gradient. The remaining profiles in the easternmost portion of the domain were too few in number to calculate meaningful statistics. Second, any profile lacking critical refraction (i.e. dN/dz < -157 N-units km^{-1}) points was excluded from the analysis which resulted in the removal of 47 radiosonde and 176 ERA5 profiles. Third, the noisy bending angle could result in errors in Abel refractivity retrieval and cause positive N-bias. Therefore, the profiles with N-bias greater than +0.5% are excluded resulting in the removal of 61 MAGIC profiles and 16 ERA5 profiles. Fourth, the profiles with only surface ducting, i.e., below 300 m threshold, are discarded. Finally, 25 radiosonde profiles and 2 ERA5 profiles were removed due to the Abel retrieval failure. After implementing all quality control measures, the number of radiosonde and ERA5 profiles used for the N-bias analysis is reduced to 396 and 319 profiles, respectively.

3.1 PBL analysis

To evaluate the ducting properties along the transect from the coast of southern California to Hawaii, we group the MAGIC radiosonde and the colocated ERA5 profiles into eight 5° longitude bins between $-160.0°$ and $-120.0°$, which allows for the spatial variation of the PBL, ducting layer and the associated properties along the transect to be easily illustrated. Figure 4 shows the median value of PBLH (a), minimum gradient (b) and sharpness parameter (c) along the transect. The median-absolute-deviation (MAD) for each parameter is also shown.

In Fig. 4a, the MAGIC radiosondes clearly show the gradual increase of the PBLH along the transect from the shallow stratocumulus-topped PBL (~800 m) near the southern California coast westward to the much deeper trade-cumulus regime (~1.8 km) near Hawaii. A similar structure is seen in the colocated ERA5 data but with an average low bias of 165 m below the radiosonde. However, a nearly 800 m underestimation in PBLH over the two westernmost bins near Hawaii is also seen, this is consistent with what is found over the equivalent trade cumulus region of the subtropical southeast Pacific Ocean (Xie et al., 2012). Such a discrepancy could be due to the sensitivity of gradient method to the vertical resolution of the data. Over the western segment of

244   the transect (near Hawaii), two major gradient layers (one at ~1 km and the other at ~2 km) with

245   comparable refractivity gradients are often observed (e.g., Fig. 2). The gradient layer at around 2

246   km is well-known as the trade-wind inversion. While the lower-level gradient layer at ~1 km, is

247   generally called a mixing layer. Note the radiosonde data exhibit consistent vertical sampling (~8

248   m resolution) below 3 km, and resolve both layers well. However, the ERA5 data have an

249   uneven vertical sampling intervals increasing with height, with 10 – 100m resolution below 1

250   km, 100 – 160 m within 1-2 km, and 160 – 200 m within 2-3 km. Therefore, the ERA5 data are

251   more likely to resolve the sharp gradient structure below 1 km than the one at higher altitude.

252   This could result in resolving the mixing layer (below 1 km) with the sharpest refractivity

253   gradient, instead of the trade-wind inversion near 2 km in the ERA5 data. Note that the larger

254   median absolute deviation for the westernmost bins compared to the rest of the transect

255   illustrates the existence of greater PBLH variability closer to the trade-cumulus boundary layer

256   regime. The westward decreasing magnitude of the minimum refractivity gradient (Fig. 4b) and

257   sharpness parameter (Fig. 4c) indicates the westward weakening of moisture lapse rate and/or

258   temperature inversion across the PBL top, which is consistent with the decreasing synoptic-scale

259   subsidence from the California coast to Hawaii (Riehl, 1979).
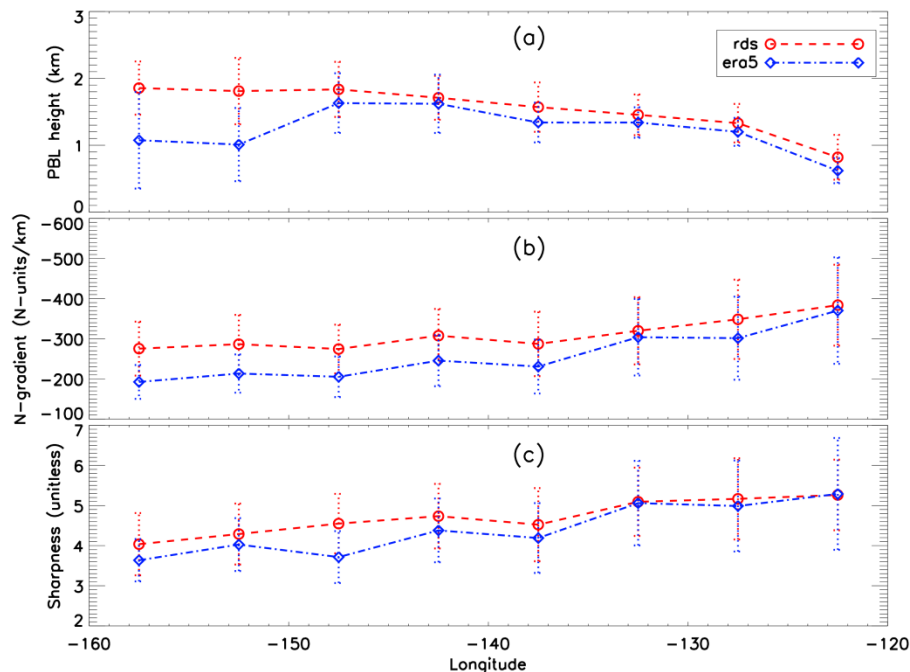
260

261 **Figure 4: Zonal transect of 5° bin MAGIC and ERA5 PBLH (a), minimum refractivity gradient (b) and sharpness**
262 **parameter (c) for MAGIC (median in red circle and dashed line, MAD in red dotted error bars) and ERA5 (median in**
263 **blue diamond and dot-dashed line, MAD in blue dotted error bars).**

264

265   It is also notable that the ERA5 systematically underestimates not only the PBLH but also the

266   magnitude of the minimum gradient across the entire transect. This can also be seen in the

267   sharpness parameter west of −132.5˚. This discrepancy could be partially attributed to the

268   decrease in vertical sampling in ERA5 profiles as compared to the radiosondes, the result of

269   which leads to a weaker PBL refractivity gradient and coincides with an increasing PBLH.

270   Therefore, the underestimation of the ERA5 minimum refractivity gradient increases in

271   magnitude from east to west and becomes most prominent near Hawaii where the PBLH reaches

272   the maximum height over the region.

273   **3.2 Ducting characteristics**

274   As introduced in Sect. 2.3, the key characteristics of the ducting layer along the transect will be

275   investigated, these include the ducting layer height, thickness (Δh), and strength (ΔN), as well as

276   the average refractivity gradient within the ducting layer ($\Delta N/\Delta h$). All parameters are

277   interpolated to a 10 m vertical grid.

278   The ducting layer heights from both radiosonde and ERA5 show a westward increase along the

279   transect is seen in Fig. 5a. Note again that the ERA5 shows a systematic ~100–200 m low bias

280   when compared to the radiosondes between −122.5˚ and −147.5˚, with the difference increasing

281   to more than 500 m near Hawaii. The ducting layer thickness is the median height from the

282   bottom of the ducting layer to the top and is expressed in km (Fig. 5b). Ducting thickness (Δh)

283   for MAGIC shows a near constant value of 110 m across the entire transect with only a slight

284   increase to 130 m at −122.5˚, consistent with Ao et al. (2003). Conversely, the ERA5 shows a

285   constant but slightly thicker ducting layer to the east of −137.5˚ and then a decreasing thickness

286   to the west of −137.5˚ (Fig. 5b).

287   The ducting layer strength is the decrease in refractivity from the bottom of the ducting layer to

288   the top (Fig. 5c) and the ratio $\Delta N/\Delta h$ reflects the average gradient of the ducting layer (Fig. 5d).

289   The ducting strength (ΔN) for the radiosondes generally ranges from 25 N-units near Hawaii to

290   40 N-units near the coast of California. Both ΔN and $\Delta N/\Delta h$ show an overall westward

291   decreasing trend along the transect which is consistent with the decrease in magnitude of the

292   refractivity gradient (Fig. 4b). Note that MAGIC and ERA5 show similar ducting strength in the

293   eastern part of the region but diverge near −137.5˚ with ERA5 10 to 20 N-units weaker than the

294   MAGIC profiles. On the other hand, ERA5 shows a systematic lower average refractivity

295   gradient (Δ*N*/Δ*h*) than MAGIC throughout the transect, indicating the challenge in ERA5 to

296   consistently resolve the sharp vertical structure in refractivity, and likewise in temperature and

297   moisture profiles, across such a thin ducting layer. The problem becomes acutely clear near the

298   trade cumulus region.
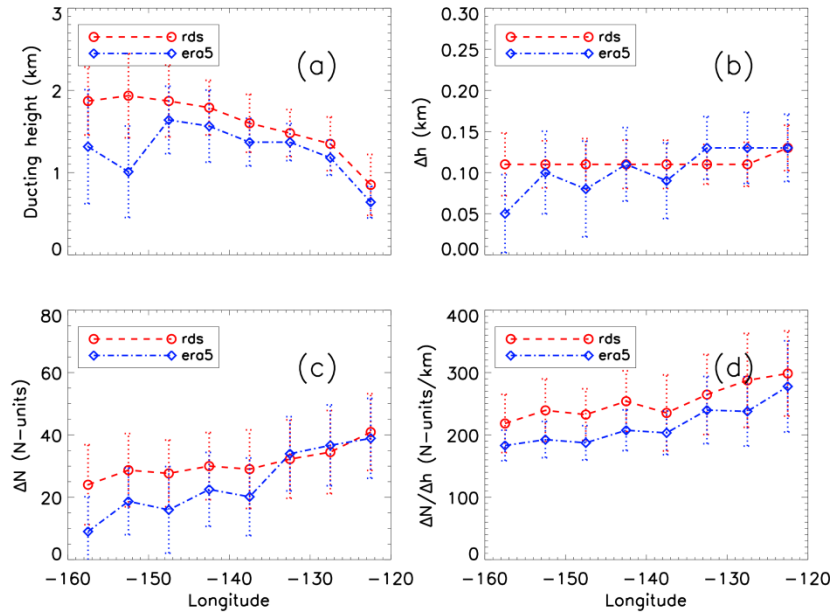
299
300   **Figure 5: Zonal transect of 5° bin median (a) ducting height, (b) ducting layer thickness (Δ*h*), (c) ducting layer strength**
301   **(Δ*N*), and (d) average ducting layer gradient Δ*N*/Δ*h* for MAGIC (median in red circle and red-dashed line, MAD in red-**
302   **dotted error bars) and ERA5 (median in blue diamond and dot-dashed line, MAD in blue-dotted error bar).**
303

304   Figure 6 shows ducting layer thickness as a function of ducting layer strength, with each data

305   point colored by its respective longitude bin. The relationship between Δ*h* and Δ*N* is not

306   longitude-dependent for either data set, but a linear trend is evident for thinner ducting layers (Δ*h*

307   < 0.1 km) with weaker ducting strength (Δ*N* < ~25 N-units). However, for the ducting layers

308   thicker than 0.1 km, such a trend becomes less identifiable, and the ducting strength Δ*N* begins to

309   show more variability toward larger values.

310
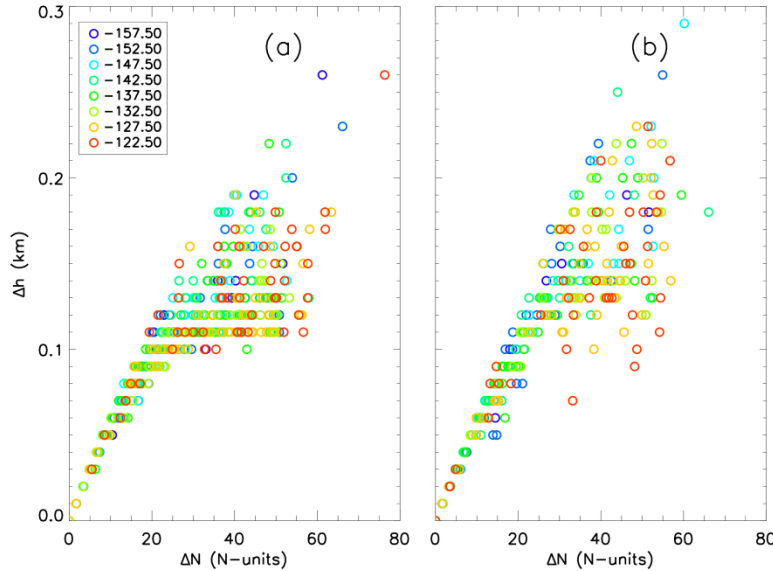
Figure 6: Comparison of individual profiles' ducting strength (ΔN) vs. ducting thickness (Δh) for MAGIC (a) and ERA5 (b). The color of each circle represents the location of the 5° longitude bin of each observation.

3.3 Ducting-induced GNSS RO *N*-bias statistics

To estimate the systematic negative *N*-bias in GNSS RO observations due to ducting, we have applied the end-to-end simulation described in sect. 2.4 to all radiosonde and ERA5 refractivity profiles with at least one elevated ducting layer detected. The *N*-bias along the transect as well as its relationship to the ducting properties are presented below.

3.3.1 Assessing ducting-induced *N*-bias

Figure 7 shows a composite of both MAGIC (396 profiles) and ERA5 (319 profiles) *N*-bias profiles which have been normalized to their PBLH, with the median *N*-bias and MAD overlaid. The systematic negative *N*-bias peaks at approximately 100 m below the PBLH and decreases at lower altitude. The peak median value of the *N*-bias for radiosondes is −5.42% (MAD, 2.92%), nearly twice the ERA5 value of −2.96% (MAD, 2.59%), indicating the significant underestimation of ducting strength in ERA5 data. However, the variabilities (MAD) of the radiosonde and ERA5 data are within 0.33% of each other, indicating that ERA5 data successfully capture the variations of ducting features seen in the radiosondes. It is worth noting that many radiosonde profiles show small negative *N*-biases above the PBLH (i.e., zero-adjusted height), which is the result of a secondary ducting layer above the major ducting layer near the

330   PBLH. Conversely, few ERA5 profiles show the presence of the secondary ducting layer above

331   PBLH.

332
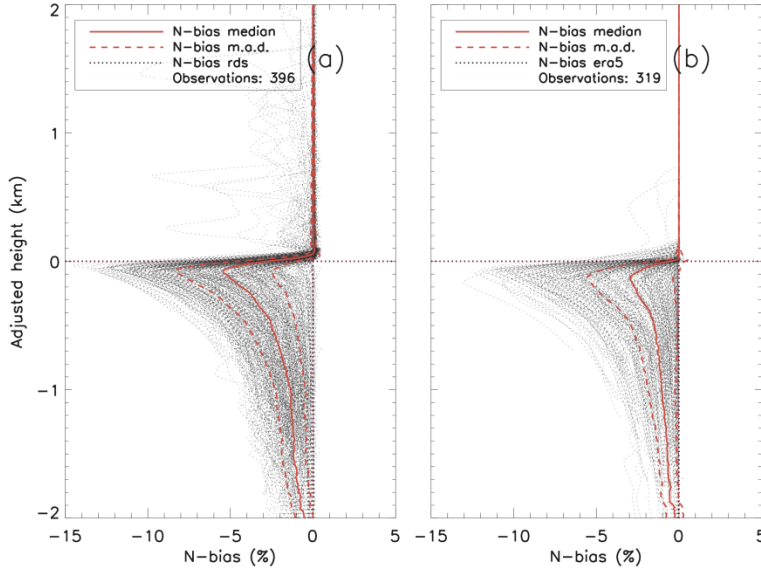
334   **Figure 7: Fractional refractivity difference (*N*-bias in %) between the simulated Abel-retrieved refractivity profile and**
335   **the original observation profile ($(N_{Abel} - N_{Obs})/N_{Obs}$), for all individual observations (dotted gray): (a) MAGIC radiosondes**
336   **(396 total profiles) and (b) ERA5 (319 total profiles) with population median (solid red) ± MAD (dashed red). Note the**
337   **zero value in the adjusted height refers to the PBLH for each individual *N*-bias profile.**

3.3.2 Zonal variation of the *N*-bias along the transect

339   To illustrate the large variation in the *N*-bias vertical structure resulting from the spatial

340   variations of ducting height and strength, Fig. 8 presents the *N*-bias profiles (median ± MAD) for

341   each 5˚ bin, replacing the zero adjusted height with the median PBLH for each bin. The

342   radiosonde composite (Fig. 8a) illustrates the westward transition of the median *N*-bias profiles

343   from the largest peak *N*-bias at ~0.8 km near the coast of Los Angeles, California, to a much

344   reduced peak *N*-bias but higher altitude of ~1.8 km at Honolulu, Hawaii. Table 1 lists detailed

345   statistics of the peak *N*-bias values at each bin for both radiosonde and ERA5 data. Although the

346   vertical structure of the *N*-bias profiles along the transect are consistent as seen in Fig. 7,

347   significant changes of the *N*-bias magnitude and its peak *N*-bias occurring height along the

348   transect are clearly seen.

349   The maximum peak *N*-bias (−7.86%) in the radiosonde data is located at the easternmost of the

350   transect near California (−122.5˚E). Whereas the minimum peak *N*-bias (−4.37%) is located near

351   the center of the transect (−147.5˚E). Similarly, the ERA5 also show the maximum peak *N*-bias

(−5.92%) near California (−122.5˚E). However, the minimum peak *N*-bias (−0.77%) is found near Hawaii (−157.5˚E). Overall, the *N*-bias in ERA5 are smaller than radiosonde in all bins. However, a noticeable difference exists between the ERA5 and radiosonde profiles for the two westernmost longitude bins (−157.5˚E and −152.5˚E) where the ERA5 reveals a much lower and weaker *N*-bias than the MAGIC data.

Note that the PBLH is above the height of the peak *N*-bias, with a maximum difference of 100 m (−137.5˚E) and a minimum difference of ~15 m (−152.5˚E). Comparatively, the ERA5 PBL height shows greater difference than the height of peak *N*-bias with a maximum difference of 230 m (−142.5˚E) and a minimum of ~45 m (−157.5˚E).
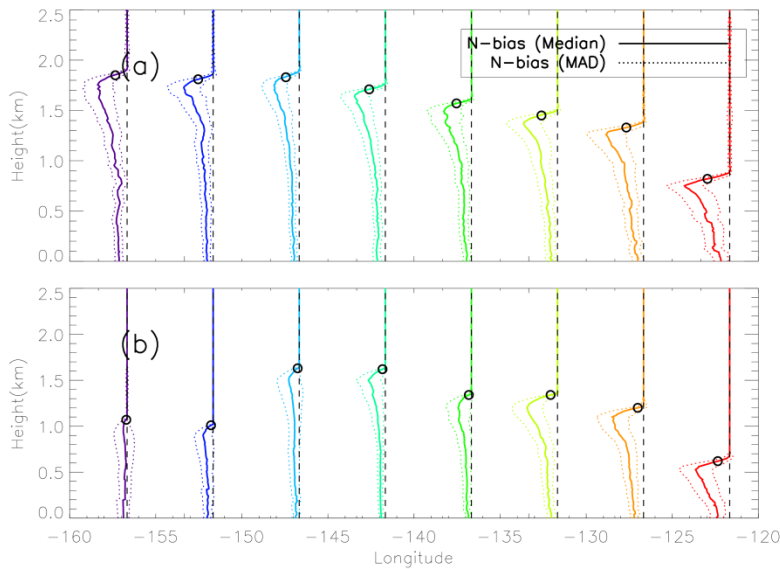
Figure 8: Median *N*-bias (solid) ± MAD (dotted) along the north Pacific transect for MAGIC radiosondes (a) and ERA5 (b). Open circles represent the median PBLH for each 5˚ bin.

Table 1: Median and MAD peak *N*-bias values for MAGIC radiosondes (RDS) and ERA5 for each 5˚ bin.

Peak N-bias				
Longitude	**RDS median**	**RDS MAD**	**ERA5 median**	**ERA5 MAD**
−157.5˚	−5.12	±2.61	−0.77	±1.73
−152.5˚	−5.10	±2.97	−1.76	±1.61
−147.5˚	−4.37	±2.14	−1.83	±2.10
−142.5˚	−5.36	±2.53	−2.95	±2.17
−137.5˚	−4.82	±2.96	−2.31	±2.14
−132.5˚	−5.90	±3.03	−5.31	±2.68
−127.5˚	−6.55	±3.40	−5.45	±2.88
−122.5˚	−7.86	±3.15	−5.92	±3.04

369   Figure 9 further illustrates the peak N-bias, median PBL N-bias (0.3 km to PBLH), and the near

370   surface N-bias (at 0.3 km) at each bin along the transect. Note the median PBL N-bias refer to the

371   median value from the near surface (0.3 km) to the PBLH. Contrary to the general trend of

372   westward decrease in magnitude of the minimum refractivity gradient (Fig. 4b) and ducting

373   strength (Fig. 5c), the radiosonde peak N-bias shows the maximum (median: −8.10%, MAD:

374   3.26%) near California (−122.5˚E) and the minimum (median: −4.85%, MAD: 2.18%) over the

375   transition region (−147.5˚E) as well as a slight increase to a secondary maximum (median:

376   −6.11%, MAD: 2.85%) near Hawaii (−157.5˚E). The median PBL N-bias and the near surface N-

377   bias also show a similar pattern. However, the median N-bias demonstrates a sharp decrease in

378   the eastern half of the domain from −5.25% (MAD: 2.71%) at −122.5˚E to −1.71% (MAD:

379   1.26%) at −137.5˚E, and then remains relatively constant over the western half of the domain.

380   Similarly, the near surface N-bias reaches a maximum magnitude of −3.54% (MAD: 2.11%),

381   sharply decreases to −1.06% (MAD: 0.85%) at −137.5˚E, and then remains relatively constant

382   over the western half of the domain.

383   Note that normalizing each N-bias profile to the PBLH preserves the magnitude of the N-bias

384   with various heights. Therefore, the relatively large normalized N-bias observed near Hawaii

385   indicates more persistent ducting over the trade-cumulus boundary layer regime compared to the

386   transition region in the middle of the transect at -147.5˚E (Fig. 8a).

387   On the other hand, the ERA5 data show a westward decrease of all three N-biases, systematically

388   underestimating all three as compared to the radiosondes. This is expected as the decrease of

389   ERA5 vertical resolution at higher altitude leads to a weaker PBL N-gradient observation (Fig.

390   4b), and thus weaker ducting and a smaller ducting-induced N-bias. Such underestimation of the

391   N-bias in the ERA5 minimizes near California where the PBLH is lowest but becomes more

392   severe westward with an increase in height, reaching a maximum magnitude N-bias difference

393   near Hawaii. In this case, the peak N-bias is merely −0.71% (MAD: 1.80%) as compared to

394   −6.23% (MAD: 2.98%) at −122.5˚E (Fig. 9a and Table 1). The large difference seen in the N-

395   bias along the transect strongly indicates the challenges of the ERA5 data to resolve the sharp

396   gradient across the ducting layer, resulting in a large variation in PBLH of the ERA5 data in the

397   western segment of the region. The increasing difference between the radiosonde and ERA5 data

398   from east to west is most pronounced in the peak N-bias cross-section (Fig. 9a) but is also

399   evident in both the median N-bias (Fig. 9b) as well as the near surface N-bias (Fig. 9c).
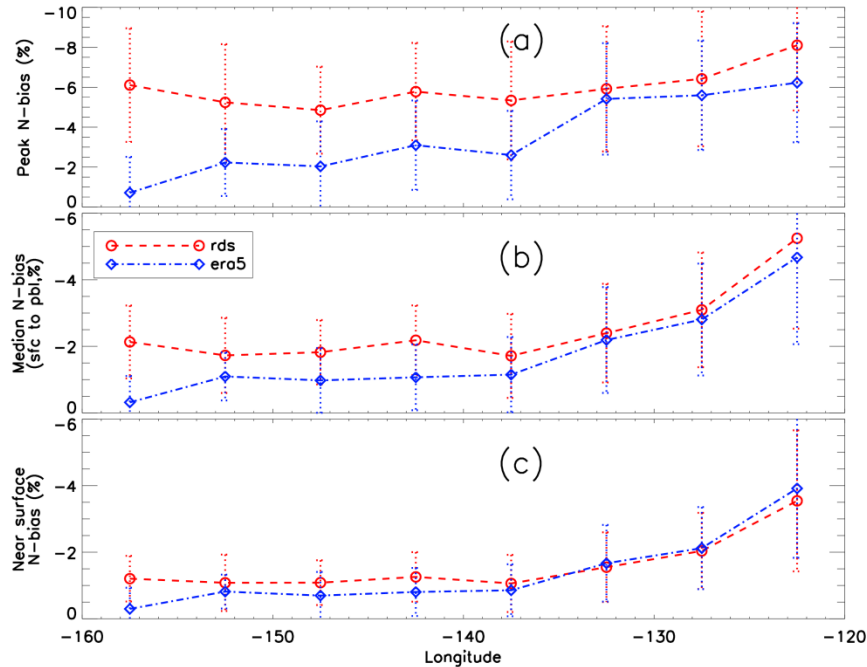
400
401 **Figure 9: Zonal transect of 5° bin (a) peak *N*-bias, (b) median PBL *N*-bias (0.3 km to PBLH), and (c) near surface *N*-bias**
402 **at 0.3 km for MAGIC (median in red circle and red-dashed line, MAD in red-dotted error bar) and ERA5 (median in**
403 **blue diamond and dot-dashed line, MAD in blue-dotted error bar)**

3.3.3 The relationship between *N*-bias and key variables

Figure 10 shows a scatter plot of the PBLH vs. height of peak *N*-bias along the transect with each data point colored by the center longitude of the bin to which it belongs. The PBLH and the height of peak *N*-bias show a clear linear relationship with high correlation for both the MAGIC (0.89) and ERA5 (0.98) data. The majority of the radiosonde data show the heights of peak *N*-bias align well with the PBLH with a very small low bias (less than 80 m). The reason for the lower correlation value in MAGIC data is attributed to outlier cases when the radiosonde *N*-bias profiles with a double peak at which the larger magnitude bias is located (Fig. 7a). On the other hand, the ERA5 maximum ducting heights show little difference from the PBLH near California (e.g., −122.5˚E), but become lower moving westward, which is illustrated by the increasing difference between the linear regression line and the 1:1 line.
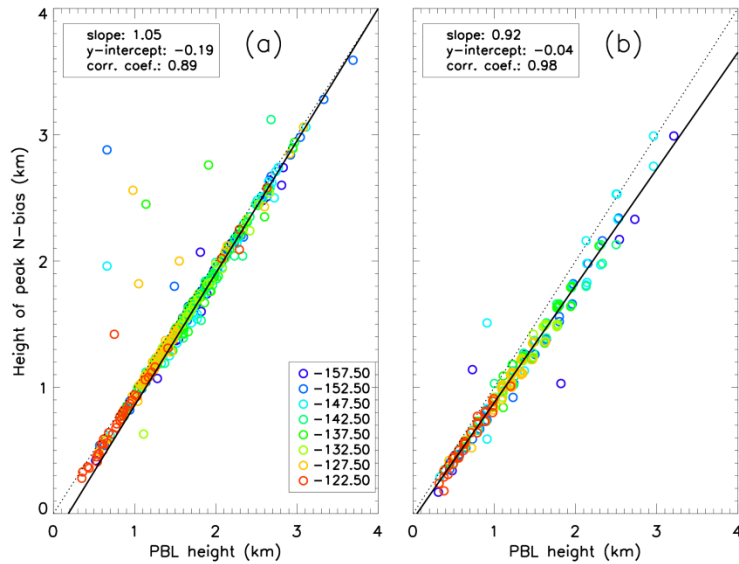
Figure 10: PBLH vs. height of peak *N*-bias for individual profiles from MAGIC (a) and ERA5 (b) data. The color of each open circle represents the center longitude of the 5° bin to which each profile belongs.

Figure 11 shows a near-linear relationship between the minimum refractivity gradients and the peak *N*-biases for both MAGIC radiosondes and ERA5 profiles, i.e., the sharper the refractivity gradient, the larger the *N*-bias. The correlation coefficient for both MAGIC radiosondes (0.93) and the ERA5 profiles (0.88) are also presented. The sharpness parameter (Fig. 11c, 11d) also shows a linear relationship with the maximum *N*-bias which is a result of its dependence on the minimum refractivity gradient. Interestingly, their relationship with the peak *N*-bias exhibits no indication of zonal dependence.
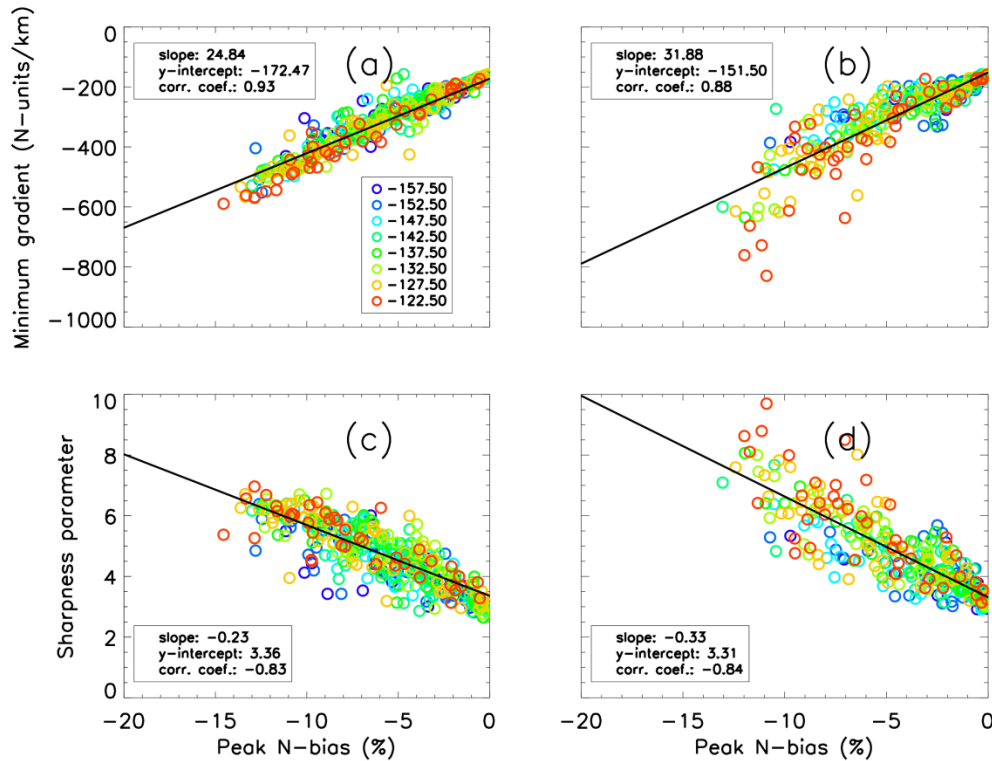
Figure 11: (a, b) Minimum refractivity gradient (N-units km⁻¹) and (c, d) sharpness parameter, as a function of the peak
N-bias (%) for MAGIC (a, c) and ERA5 (b, d) data with the line of linear regression in solid black. Color of each open
circle represents the center longitude of the 5° bin to which each profile belongs.

4   Summary and Conclusions

In this study, radiosonde profiles from the MAGIC field campaign have been analyzed to
investigate ducting characteristics and the induced systematic refractivity biases in GNSS RO
retrievals over the Northeastern Pacific Ocean between Hawaii and California. Colocated ERA5
model reanalysis data were used as a secondary comparison to the radiosonde observations.

The nearly 1-year high-resolution MAGIC radiosonde dataset reveals the frequent presence of
ducting marked by a sharp refractivity gradient resulting from the large moisture lapse rate
across a strong temperature inversion layer. The PBLH increases by more than 1 km along the
transect from California to Hawaii while the magnitude of the refractivity gradient decreases by
100 N-units km⁻¹. The zonal gradient of both variables illustrates the transition of the PBL from
shallow stratocumulus adjacent to the California coast to deeper trade-wind cumulus that are
prevalent near the Hawaiian Islands.

End-to-end simulation on all radiosonde and ERA5 refractivity profiles has been conducted to
estimate the systematic negative *N*-bias in GNSS RO observations. The ducting layer maintains

445   remarkably consistent thickness (110 m) along the transect with westward decreasing strength

446   and increasing height. The ERA5 slightly underestimates both the height and strength of the

447   ducting layer as well as the PBLH. A systematic negative refractivity bias (N-bias) below the

448   ducting layer is observed throughout the transect, peaking (-5.42%) approximately 80 meters

449   below the PBL height, and gradually decreasing towards the surface (-0.5%). The height of the

450   peak N-bias and the PBLH show a highly positive correlation. The median difference between

451   the two is about 80 meters in the radiosonde but increasing to about 120 meters in the colocated

452   ERA5 data.

453   MAGIC radiosondes indicate larger values of both ducting strength (ΔN) and thickness (Δh) than

454   ERA5 in the western half of the transect. The opposite is true in the eastern portion of the

455   domain, and is likely associated with the transition of the cloud layer from open-cell cumulus in

456   the west to stratocumulus and stratus in the east (Bretherton et al., 2019; Wood et al., 2011). The

457   ERA5 systematically underestimates the average ducting layer gradient ($\Delta N/\Delta h$) comparing to

458   the radiosondes. The largest N-bias is found over the region with strongest ducting and largest

459   sharpness parameter. It is worth noting that the PBL over the western portion of the transect near

460   Hawaii frequently shows two major gradient layers (a mixing layer at ~1 km and the trade-

461   inversion at ~2 km), with comparable N-gradients (e.g., Fig. 2). The much lower PBLH seen in

462   ERA5 in this region is likely due, in part, to the decreasing number of model levels in ERA5 at

463   higher altitude, which could lead to higher possibility of identifying the lower gradient layer as

464   the PBLH. However, the impact of the vertical resolution on the performance of gradient method

465   for PBLH detection has not been performed in this study and warrants more comprehensive

466   study in the future.

467

468

469

470

471

472

473

474

475

5   Data availability

Data for the Marine Atmospheric Radiation Measurement (ARM) GCSS Pacific Cross Section Intercomparison (GPCI) Investigation of Clouds (MAGIC, Zhou et al., 2015) can be accessed through the U.S. Department of Energy's Office of Science https://www.arm.gov/research/campaigns/amf2012magic.

Data for the ECMWF Reanalysis version 5 (ERA5, Hersbach et al., 2020) can be accessed at https://www.ecmwf.int/en/forecasts/dataset/ecmwf-reanalysis-v5.

6   Author contribution

Author Thomas Winning is responsible for all original text and, data analysis and production of graphics. Author Kevin Nelson contributed by providing updated data processing code, colocation of ERA5 data with MAGIC observations and first and second round edits. Author Feiqin Xie is the academic advisor for the primary author and also provided draft edits and paper organization and writing guidance.

7   Competing interests

The authors declare no competing interests, see Acknowledgements for current affiliation.

8   Acknowledgements

The authors acknowledge funding support of earlier work from NASA grant (NNX15AQ17G). Authors T. Winning and K. Nelson were also partially supported by research assistantship from Coastal Marine System Science Program at Texas A&M University – Corpus Christi. The high-resolution ERA5 reanalysis data were acquired from ECMWF and the Climate Data Service (CDS). The MAGIC radiosonde data were provided by the Atmospheric Radiation Measurement program (ARM) Climate Research Facility sponsored by the U.S. Department of Energy (DOE). Author T. Winning's current affiliation: Ventura County Air Pollution Control District, Ventura, CA, 93003, USA. Author T. Winning acknowledges this work was done as an academic pursuit in association with Texas A&M University – Corpus Christi and not in the author's capacity as an employee of the Ventura County Air Pollution Control District.

Author K. Nelson's current affiliation: Jet Propulsion Laboratory, California Institute of Technology, Pasadena, CA, 91109, USA. Author K. Nelson acknowledges this work was done as a private venture and not in the author's capacity as an employee of the Jet Propulsion Laboratory, California Institute of Technology.

References

Anthes, R. A., and Coauthors: The COSMIC/FORMOSAT-3 Mission: Early Results, BAMS, 89, 313–334, doi.org/10.1175/bams-89-3-313, 2008.

Ao, C. O., Meehan T. K., Hajj, G. A., Mannucci, A. J., and Beyerle, G.: Lower Troposphere Refractivity Bias in GPS Occultation Retrievals, J. Geophys. Res., 108, 4577, doi:10.1029/2002JD003216, 2003.

Ao, C. O.: Effect of Ducting on Radio Occultation Measurements: An Assessment Based on High-resolution Radiosonde Soundings, Radio Sci., 42, RS2008, doi.org/10.1029/2006RS003485, 2007.

Ao, C. O., Chan, T. K., Iijima, A., Li, J.-L., Mannucci, A. J., Teixeira, J., Tian, B., and Waliser, D. E.: Planetary Boundary Layer Information from GPS Radio Occultation Measurements, in: Proceedings of the GRAS SAF Workshop on Applications of GPSRO Measurements, Vol. 5 of, GRAS SAF Workshop on Applications of GPSRO Measurements, Reading, United Kingdom, ECMWF and EUMETSAT, 123–131, https://www.ecmwf.int/sites/default/files/elibrary/2008/7459-planetary-boundary-layer-information-gps-radio-occultation-measurements.pdf, 16–18 June, 2008.

Ao, C. O., Waliser, D. E., Chan, S. K., Li, J.-L., Tian, B., Xie, F., and Mannucci, A. J.: Planetary boundary layer heights from GPS radio occultation refractivity and humidity profiles, J. Geophys. Res., 117, D16117, doi:10.1029/2012JD017598, 2012.

Basha, G., and Ratnam, M. V.: Identification of atmospheric boundary layer height over a tropical station using high-resolution radiosonde refractivity profiles: Comparison with GPS radio occultation measurements, J. Geophys. Res., 114, doi.org/10.1029/2008jd011692, 2009.

Beyerle, G., Gorbunov, M. E., and Ao, C.O.: Simulation studies of GPS radio occultation measurements, Radio Sci., 38, 1084, doi:10.1029/2002RS002800, 2003.

Bretherton, C.S., and Coauthors: Cloud, Aerosol, and Boundary Layer Structure across the Northeast Pacific Stratocumulus–Cumulus Transition as Observed during CSET, Mon.Wea. Rev., 147, 2083–2102. DOI: 10.1175/MWR-D-18-0281, 2019

538

539 Eshleman, V.R.: The radio occultation method for the study of planetary atmospheres, Planet. Space Sci., 21, 1521-

540 1531, doi.org/10.1016/0032-0633(73)90059-7, 1973.

541

542 Feng, X., Xie, F., Ao, C.O., and Anthes, R.A.: Ducting and Biases of GPS Radio Occultation Bending Angle and

543 Refractivity in the Moist Lower Troposphere, J. Atmos. Oceanic Technol., 37, 1013–1025, doi.org/10.1175/JTECH-

544 D-19-0206.1, 2020.

545

546 Fjeldbo, G., and Eshleman, V.R.: The Atmosphere of Mars Analyzed by Integral Inversion of the Mariner IV

547 Occultation Data, Planet. Space Sci., 16, 1035-1059, doi.org/10.1016/0032-0633(68)90020-2, 1968.

548

549 Fjeldbo, G., Kliore, A.J., and Eshleman, V.R.: The Neutral Atmosphere of Venus as Studied with the Mariner V

550 Radio Occultation Experiment, Astron. J., 76, 123-140, doi.org/10.1086/111096, 1971.

551

552 Garratt, J. R.: Review: the atmospheric boundary layer, Earth-Sci. Rev., 37, 89–134, 1994

553

554 Guo, P., Kuo, Y. H., Sokolovskiy, S. V., and Lenschow, D. H.: Estimating Atmospheric Boundary Layer Depth

555 Using COSMIC Radio Occultation Data, J. Atmos. Sci., 68, 1703–1713, doi.org/10.1175/2011jas3612.1, 2011.

556

557 Gorbunov, M. E.: Canonical transform method for processing radio occultation data in the lower troposphere, Radio

558 Sci., 37(5), 1076, doi:10.1029/2000RS002592, 2002.

559
560 Gorbunov, M. E., Benzon, H. H., Jensen, A.S, Lohmann, M.S., and Nielsen, A.S.: Comparative analysis of radio

561 occultation processing approaches based on Fourier integral operators. Radio Sci., 39, RS6004,

562 https://doi.org/10.1029/2003RS002916, 2004

563

564 Healy, S. B.: Radio occultation bending angle and impact parameter errors caused by horizontal refractive index

565 gradients in the troposphere: A simulation study, J. Geophys. Res, 106, D11, 11875–11889,

566 doi:10.1029/2001JD900050, 2001.

567

568 Hersbach, H., Bell, B., Berrisford, P., Hirahara, S., Horányi, A., Muñoz-Sabater, J., Nicolas, J., Peubey, C., Radu,

569 R., Schepers, D., Simmons, A., Soci, C., Abdalla, S., Abellan, X., Balsamo, G., Bechtold, P., Biavati, G., Bidlot, J.,

570 Bonavita, M., De Chiara, G., Dahlgren, P., Dee, D., Diamantakis, M., Dragani, R., Flemming, J., Forbes, R.,

571 Fuentes, M., Geer, A., Haimberger, L., Healy, S., Hogan, R. J., Hólm, E., Janisková, M., Keeley, S.,

572 Laloyaux, P., Lopez, P., Lupu, C., Radnoti, G., de Rosnay, P., Rozum, I., Vamborg, F., Villaume, S., and Thépaut,

573 J.-N.: The ERA5 Global Reanalysis, Q. J. Roy. Meteor. Soc., 146, 1999–2049, https://doi.org/10.1002/qj.3803,

574 2020.

575

Ho, S.-P., Peng, L., Anthes, R. A., Kuo, Y.-H., and Lin, H.-C.: Marine boundary layer heights and their longitudinal, diurnal and inter-seasonal variability in the southeast Pacific using COSMIC, CALIOP, and radiosonde data. J. Climate, 28, 2856–2872, https://doi.org/10.1175/JCLI-D-14-00238.1, 2015.

Jensen, A. S., Lohmann, M.S., Nielsen, A.S. and Benzon, H.-H.: Geometrical optics phase matching of radio occultation signals, Radio Sci., 39, RS3009, doi:10.1029/2003RS002899, 2004.

Jensen, A. S., Lohmann, M.S., Benzon, H.-H, and Nielsen, A.S.: Full spectrum inversion of radio occultation signals, Radio Sci., 38(3), 1040, doi:10.1029/2002RS002763, 2003.

Johnston, B. R., Xie, F., and Liu, C.: The effects of deep convection on regional temperature structure in the tropical upper troposphere and lower stratosphere, J. Geophys. Res.: Atmos., 123, 1585−1603, doi.org/10.1002/2017JD027120, 2018.

Klein, S. A., and Hartmann, D. L.: The seasonal cycle of low stratiform clouds. Journal of Climate, 6, 1587−1606, doi:10.1175/1520-0442(1993)006<1587:TSCOLS>2.0.CO;2, 1993.

Kursinski, E. R., Hajj, G. A., Schofield, J. T., Linfield, R. P., and Hardy, K. R.: Observing Earth's atmosphere with radio occultation measurements using the Global Positioning System, J. Geophys. Res.: Atmos., 102, 23429−23465, doi.org/10.1029/97jd01569, 1997.

Kursinski, E. R., G. A. Hajj, Leroy, S. S., and Herman, B.: The GPS Radio Occultation Technique. Terr. Atmos. Ocean. Sci. (TAO), 11, 53−114, 2000.

Lewis, E. R.: Marine ARM GPCI Investigation of Clouds (MAGIC) Field Campaign Report. U.S. Department of Energy, https://doi.org/10.2172/1343577, 2016.

Maddy, E. S. and Barnet, C. D.: Vertical resolution estimates in version 5 of AIRS operational retrievals. IEEE Transactions on Geoscience and Remote Sensing, 46, 2375−2384, doi:10.1109/TGRS.2008.917498, 2008.

Nelson, K. J., Xie, F., Ao, C. O., and Oyola-Merced, M. I.: Diurnal Variation of the Planetary Boundary Layer Height Observed from GNSS Radio Occultation and Radiosonde Soundings over the Southern Great Plains. J. Atmos. Oceanic Tech., 38, 2081−2093, https://doi.org/10.1175/jtech-d-20-0196.1, 2021.

Nelson, K. J., Xie, F., Chan, B. C., Goel, A., Kosh, J., Reid, T. G. R., Snyder, C. R., and Tarantino, P. M.: GNSS Radio Occultation Soundings from Commercial Off-the-Shelf Receivers Onboard Balloon Platforms, Atmos. Meas. Tech., https://doi.org/10.5194/amt-2022-198, 2022.

614   Painemal, D., Minnis, P., and Nordeen, M.: Aerosol variability, synoptic-scale processes, and their link to the cloud
615   microphysics over the northeast Pacific during MAGIC, J. Geophys. Res. Atmos., 120, 5122–5139,
616   doi:10.1002/2015JD023175, 2015.
617

618   Patterson, W. L.: Climatology of Marine Atmospheric Refractive Effects: A Compendium of the Integrated
619   Refractive Effects Prediction System (IREPS) Historical Summaries. Naval Ocean Systems Center,
620   https://apps.dtic.mil/sti/pdfs/ADA155241.pdf, 1982.
621

622   Ramanathan, V., Cess, R. D., Harrison, E. F., Minnis, P., Barkstrom, B. R., Ahmad, E., and Hartmann, D.: Cloud-
623   radiative forcing and climate: Results from the Earth Radiation Budget Experiment, Science, 243, 57–63,
624   DOI:10.1126/science.243.4887.57, 1989.
625

626   Riehl, H.: Climate and weather in the tropics. London: Academic Press. 611 pp. ISBN 0.12.588180.0
627

628   Rocken, C., Anthes, R., Exner, M., Hunt, D., Sokolovskiy, S., Ware, R., Gorbunov, M., Schreiner, W., Feng
629   D., Herman B., Kuo, Y.-H., Zou, X.: Analysis and validation of GPS/MET data in the neutral atmosphere. J.
630   Geophys. Res., 102, 29849−29866, https://doi.org/10.1029/97JD02400, 1997.
631

632   Schreiner, W. S., Weiss, J.P., Anthes, R.A., Braun, J., Chu, V., Fong, J., Hunt, D., Kuo, Y.-H., Meehan, T.,
633   Serafino, W., Sjoberg, J., Sokolovskiy, C., Talaat, E., Wee, T.K., Zeng, Z.: COSMIC-2 Radio Occultation
634   Constellation: First Results. Geophys. Res. Lett., 47, https://doi.org/10.1029/2019gl086841, 2020.
635

636   Seidel, D. J., Ao, C.O. and Li, K.: Estimating climatological planetary boundary layer heights from radiosonde
637   observations: Comparison of methods and uncertainty analysis, J. Geophys. Res., 115, D16114,
638   doi:10.1029/2009JD013680, 2010.
639

640   Smith, E. K. and Weintraub, S.: The Constants in the Equation for Atmospheric Refractivity Index at Radio
641   Frequencies. Proc. IRE, 41, 1035−1037, doi:10.1109/JRPROC.1953.274297, 1953.
642

643   Sokolovskiy, S. V.: Modeling and Inverting Radio Occultation Signals in the Moist Troposphere. Radio Sci., 36,
644   441−458, https://doi.org/10.1029/1999RS002273, 2001.
645

646   Sokolovskiy, S. V.: Effect of super refraction on inversions of radio occultation signals in the lower troposphere.
647   Radio Sci., 38 (3), https://doi.org/10.1029/2002RS002728, 2003.
648

Sokolovskiy, S. V., Kuo, Y.-H., Rocken, C., Schreiner, W. S., Hunt, D. and Anthes, R. A., 2006: Monitoring the atmospheric boundary layer by GPS radio occultation signals recorded in the open-loop mode. Geophys. Res. Lett., 33, L12813, doi:10.1029/2006GL025955, 2006.

Stull, R., Santoso, E., Berg, L. K., and Hacker, J.: Boundary Layer Experiment 1996 (BLX96), BAMS, 78, 1149−1158, doi: 10.1175/1520-0477(1997)078<1149:BLEB>2.0.CO;2, 1997.

Stull, R. B.: An Introduction to Boundary Layer Meteorology. Kluwer Academic Publishers, 666 pp., ISBN 90-277-2768-6, 1988.

von Engeln, A. and Teixeira, J.: A Planetary Boundary Layer Height Climatology Derived from ECMWF Reanalysis Data, J. Climate, 26, 6575−6590, https://doi.org/10.1175/jcli-d-12-00385.1, 2013.

Winning, T. E., Chen, Y.-L., and Xie, F.: Estimation of the marine boundary layer height over the central North Pacific using GPS radio occultation, Atmospheric Research, 183, 362−370, https://doi.org/10.1016/j.atmosres.2016.08.005, 2017.

Wood, R., Mechoso, C. R., Bretherton, C. S., Weller, R. A., Huebert, B., Straneo, F., Albrecht, B. A., Coe, H., Allen, G., Vaughan, G., Daum, P., Fairall, C., Chand, D., Gallardo Klenner, L., Garreaud, R., Grados, C., Covert, D. S., Bates, T. S., Krejci, R., Russell, L. M., de Szoeke, S., Brewer, A., Yuter, S. E., Springston, S. R., Chaigneau, A., Toniazzo, T., Minnis, P., Palikonda, R., Abel, S. J., Brown, W. O. J., Williams, S., Fochesatto, J., Brioude, J., and Bower, K. N.: The VAMOS Ocean-Cloud-Atmosphere-Land Study Regional Experiment (VOCALS-REx): goals, platforms, and field operations, Atmos. Chem. Phys., 11, 627−654, https://doi.org/10.5194/acp-11-627-2011, 2011.

Xie, F., Syndergaard, S., Kursinski, E. R., and Herman, B.M.: An Approach for Retrieving Marine Boundary Layer Refractivity from GPS Occultation Data in the Presence of Super-refraction. J. Atmos. Oceanic Technol., 23, 1629−1644, https://doi.org/10.1175/JTECH1996.1, 2006.

Xie, F., Haase, J. S., and Syndergaard, S.: Profiling the Atmosphere Using the Airborne GPS Radio Occultation Technique: A Sensitivity Study. IEEE Transactions on Geoscience and Remote Sensing, 46, 3424−3435, https://doi.org/10.1109/tgrs.2008.2004713, 2008.

Xie, F., Wu, D. L., Ao, C. O., Kursinski, E. R., Mannucci, A. J., and Syndergaard, S.: Super-refraction effects on GPS radio occultation refractivity in marine boundary layers, Geophys. Res. Lett., 37, https://doi.org/10.1029/2010gl043299,_2010.

685 Xie, F., Wu, D. L., Ao, C. O., Mannucci, A. J., and Kursinski, E. R.: Advances and limitations of atmospheric
686 boundary layer observations with GPS occultation over southeast Pacific Ocean, Atmos. Chem. Phys., 12, 903−918,
687 doi:10.5194/acp-12-903-2012, 2012.

688

689 Zhou, X., Kollias, P., and Lewis, E.: Clouds, precipitation and marine boundary layer structure during MAGIC. J.
690 Climate, 28, 2420−2442, https://doi.org/10.1175/JCLI-D-14-00320.1, 2015.